Journal of Power Sources 205 (2012) 290–300

Contents lists available at SciVerse ScienceDirect

Journal of Power Sources

journal homepage: www.elsevier.com/locate/jpowsour

Effect of open circuit voltage on degradation of a short proton exchange membrane fuel cell stack with bilayer membrane configurations

Shengsheng Zhang[a], Xiao-Zi Yuan[a,**], Renate Hiesgen[b], K. Andreas Friedrich[c], Haijiang Wang[a,*], Mathias Schulze[c], Andrea Haug[c], Hui Li[a]

[a] Institute for Fuel Cell Innovation, National Research Council Canada, Vancouver, BC, Canada V6T 1W5
[b] University of Applied Sciences Esslingen, Department of Basic Science, Kanalstrasse 33, 73728 Esslingen, Germany
[c] Institute of Technical Thermodynamics, German Aerospace Center, Pfaffenwaldring 38-40, 70569 Stuttgart, Germany

ARTICLE INFO

Article history:
Received 18 November 2011
Received in revised form
22 December 2011
Accepted 1 January 2012
Available online 21 January 2012

Keywords:
PEM fuel cell
Twin-CCM
Degradation
Membrane
Open circuit voltage

ABSTRACT

In the present work, membrane electrode assembly degradation of a 4-cell stack with specially designed twin catalyst coated membranes (twin-CCMs) was carried out for 1600 h under open circuit voltage (OCV) conditions. Four types of membrane with various thicknesses were employed in the experiment. Each twin-CCM was composed of two membranes of the same type with a catalyst layer coated only on one side. The purpose of this special configuration was to facilitate postmortem analysis of the membrane after degradation due to the detachable membrane structure. By means of several in situ electrochemical measurements, the performance of the individual cells was analysed every 200 h during the degradation process. Postmortem analyses such as scanning electron microscopy, atomic force microscopy, and infrared imaging were also conducted to identify the membrane degradation mechanisms after exposure to OCV. The results indicate that membrane degradation, which correlates with electrode degradation, is the most direct reason for the failure of the whole cell/stack during OCV operation, especially for cells with thinner membranes.

1. Introduction

Durability and cost are recognized as two of the main barriers to the extensive application of proton exchange membrane (PEM) fuel cells as a promising clean energy technology. To date, considerable effort has been made to study their performance and component degradation via diverse accelerated test methods. Among these methods, OCV is one of the most frequently employed stressors for PEM fuel cell accelerated testing. Considerable research effort has been applied to this topic recently [1–5]. Generally, two factors are of primary consideration in the OCV degradation process. First, as we know, high potential is influential on cell performance and durability, due to dissolution/migration of the Pt catalyst and oxidation of the carbon support, which can be confirmed by a significant decrease in the electrochemical surface area (ECSA) [6]. Second, due to zero consumption of the reactant under OCV, the relatively higher reaction gas concentration is another factor causing the high degradation rate of the membrane. An elevated gas crossover rate through the membrane results in a higher peroxide radical concentration, which in turn causes a more serious chemical decomposition of the membrane [7]. High fluoride emission rates (FER) from effluent water, as well as serious membrane thinning, have also been considered evidence of PEM degradation under OCV, correlating to losses in both OCV and cell performance [3,8].

Given the current research developments in PEM fuel cell degradation under OCV, further understanding is certainly required, especially regarding the correlations between various causes of degradation. Experimental investigations into the degradation mechanisms of different components and their complex interdependence with operating conditions are increasingly being correlated with modeling activities to gain improved understanding. For example, based on a theoretical model of mixed potential, Vilekar and Datta [9] suggested that both hydrogen crossover and the resulting oxygen reduction reaction (ORR) overpotential at the cathode play critical roles in OCV. More recently, Yoon and Huang [10] have carried out an experiment at low relative humidity and high temperature under OCV. They exposed the fuel cell (with homemade bilayer MEAs) to OCV under two gas feeding conditions, hydrogen/air and 4% hydrogen/oxygen. The bilayer MEA was separable into two pieces of one-side coated membranes to facilitate the corresponding analysis. In addition to in situ electrochemical analysis, they performed postmortem examination, including uniaxial mechanical testing, infrared (IR) spectroscopy, scanning electron microscopy (SEM), and energy-dispersive X-ray

* Corresponding author. Tel.: +604 221 3038; fax: +604 221 3001.
** Corresponding author. Tel.: +604 221 3000x5576; fax: +604 221 3001.
E-mail addresses: xiao-zi.yuan@nrc.gc.ca (X.-Z. Yuan), haijiang.wang@nrc-cnrc.gc.ca (H. Wang).

0378-7753/$ – see front matter. Crown Copyright © 2012 Published by Elsevier B.V. All rights reserved.
doi:10.1016/j.jpowsour.2012.01.031

(EDX) spectroscopy to detect the degradation processes. The results suggested that highly localized degradation occurs, and a Pt band is observable within the membrane.

In our research activities, we have performed several experiments under OCV or idle conditions; both single cells and cell stacks were involved in previous experiments [11–13]. The results of the previous measurements clearly revealed accelerated degradation of membranes and electrodes under higher potential conditions. However, other factors, such as cell design and component selection, can also influence the degradation rate of PEM fuel cells.

In this study, we report degradation testing on a 4-cell stack with Nafion® membranes of different thicknesses, to build on the previous knowledge obtained in OCV studies. A twin catalyst coated membrane (CCM) configuration was applied to each cell of the stack. Each twin-CCM was composed of two semi-CCMs (i.e., catalyst coated on one side of the membrane), with the uncoated sides facing each other. The purpose of this special configuration was to facilitate postmortem analysis of the membrane after degradation occurred due to the detachable membrane structure. An additional benefit of this configuration was that the initial position of the membrane center was identifiable. Using both in situ and ex situ diagnostic tools, this stack's degradation under OCV for 1600 h was investigated. In situ characterizations included polarization curve (V(I) curve), electrochemical impedance spectroscopy (EIS), cyclic voltammetry (CV), and linear sweep voltage scans (LSV). For ex situ diagnosis, SEM is generally used to observe morphological changes after degradation, but its significance is strengthened by combining it with additional analytical methods. Therefore, in this study, the CCMs were characterized after operation using ex situ diagnostic tools like SEM, as well as IR imaging and atomic force microscopy (AFM). The combined analysis improves our understanding of degradation, especially as it occurs in the membrane.

2. Experimental

2.1. Test setup

The cell used for the OCV degradation experiment was a 4-cell PEM fuel cell stack, each cell having a 50 cm^2 active area. The materials used were commercially available products as described below:

For the gas diffusion layers (GDLs), SIGRACET 25BC from SGL Technologies was employed at the cathode. The GDL 25BC contained 5 wt% PTFE. At the anode, a GDL SIGRACET 25DC with 20 wt% PTFE loading was used. Both GDLs were coated with a microporous layer (MPL).

Ion Power customized semi-CCMs with a catalyst layer on one side of the membrane were combined to form complete membrane electrode assemblies (MEAs). The Pt loading was 0.3 mg cm^{-2} in the catalyst layer. The membranes used were N117, N115, N212, and N211.

The schematic diagram of these twin-CCMs is shown in Fig. 1. The MEAs were formed by sandwiching the Kapton film sealed twin-CCMs between the anode and cathode GDLs. Graphite bipolar plates were used, containing a water flow field on the back to thermalize the cell at a constant temperature. The aligned cell stack was then compressed uniformly under 100 Psi (689,475.7 Pa) using nitrogen, and connected with an Arbin 500 W fuel cell test station. The anode and cathode gases followed a counter flow pattern for all of the 4 cells in the stack during the test.

2.2. Experiment procedure

Conditioning was performed in the test station. The stack was checked for gas leakages before conditioning by load cycling

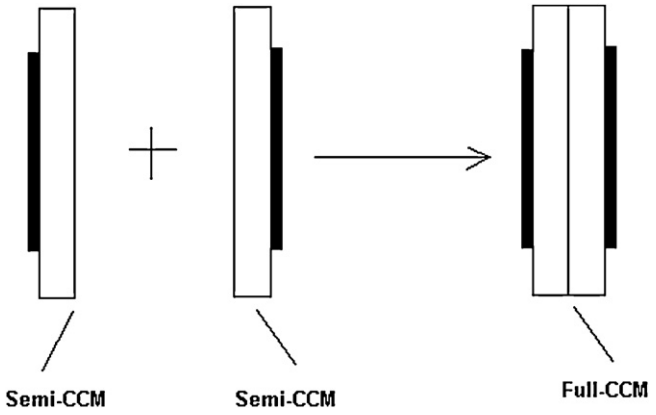

Fig. 1. Schematic diagram of the twin-CCM.

(described below). The 4 cells within the stack were named Cell 1 (with N117 membrane), Cell 2 (with N115 membrane), Cell 3 (with N212 membrane), and Cell 4 (with N211 membrane), from the bottom to the top. Each current cycle of the conditioning process consisted of OCV for 10 min, constant current at 20 A for 30 min, and constant current at 10 A for 30 min. The cycle was repeated for a total of 22 h until there was no further performance improvement for at least 3 h.

The fuel cell temperature was kept at 70 °C using an externally heated circulator. Air and hydrogen were fully humidified in bubblers at 70 °C before their entrance into the fuel cell. Both anode and cathode were under ambient pressure during the entire experiment. Note that all the temperature settings for the following tests were the same to ensure constant conditions. The stoichiometries for air and hydrogen were set at 2.5 and 1.5, respectively. The minimum flow rates for air and hydrogen were about 2 slpm (standard litre per minute) and 1 slpm, respectively.

The electrochemical characteristics measured after the conditioning processes were regarded as the baseline data. The current and voltage data were recorded with the Arbin test station. For impedance testing, a Solartron SI-1260 impedance/gain-phase analyzer was used in combination with a Solartron SI-1287 electrochemical interface, in the frequency range of 10 kHz to 0.1 Hz and with an excitation amplitude of 10 mV. For the CV and LSV tests, the cathode gas was switched to nitrogen to record the ECSA and the hydrogen crossover rate, respectively. Therefore, the anode side remained under hydrogen feed and the flow rates for nitrogen and hydrogen were kept constant at 2 slpm and 1 slpm, respectively. In this case, the anode served as both the reference and counter electrodes, and the cathode served as the working electrode. The cycling was performed between 0.05 and 1.2 V vs. reversible hydrogen electrode (RHE) at a scan rate of 50 mV s^{-1}. The ECSA was calculated based on the catalyst loading and the total charge area of the hydrogen desorption/absorption peak integrated from about 0.1 V to 0.4 V (vs. RHE), after subtracting the double layer charge on the CV curves. During LSV measurement, all the operating conditions for the fuel cell were the same as in the CV test, except for the application of a linear potential scan from 0.05 to 0.5 V on the cathode at a scan rate of 5 mV s^{-1}.

It is also worth noting that the applicable electrochemical evaluation tests conducted in this experiment all referred to the cathode side. These electrochemical diagnoses were then performed at the end of each 200 h of OCV holding. After 1200 h of degradation and corresponding tests, the whole test setup was moved to another test station with the same function due to the scheduling of the test stations. Therefore, the last 400 h of OCV holding and the last two electrochemical tests were finished on the second test station.

Apart from these electrochemical measurements, fluoride release data was also collected every 200 h to analyse the effluent water (both anode and cathode) using a fluoride ion selective electrode.

As a postmortem measurement, IR imaging was conducted on the degraded MEAs to detect whether any pinholes were generated after the degradation test. An IR camera (InfraTech GmbH) was employed in this test. The degraded MEAs removed from the degradation cells were installed one by one in a dummy cell with an open cathode. Hydrogen passed through the anode side at a flow rate of 0.1 slpm at room temperature. The IR camera was placed on the cathode side to observe the temperature distribution of each individual cell under the same gas flow rate and room temperature. The principle of measuring temperature distribution using IR imaging is based on the heat output from the chemical reaction between hydrogen and oxygen in the presence of Pt catalyst, demonstrating the level of reactant crossover through the PEM. For comparison, the same test was also conducted on fresh MEAs with the same twin-CCM configuration.

To identify membrane thickness changes, cross-sectional SEM images were taken after degradation, using a HITACHI S-3500 N SEM. In addition, the Pt content of the membranes was analysed using high-resolution SEM-EDX (LEO 982 GEMINI) at 6 different sites of the cross-sections of each MEA.

AFM was performed using a Multimode 8 system with two different tapping mode techniques. In the "HarmoniX" mode (Bruker Corp.), a specially designed asymmetrical AFM tip is needed, which enhances the higher harmonic oscillation after contact with the sample surface. From these oscillations, the force–distance curve can be reconstructed at every image point. Adhesion force, energy dissipation, phase shift, stiffness, and peak force can be evaluated together with the topography, but no current measurement is possible because the special tip is not conductive [14–17]. In the "Quantitative Nanomechanical Peak Force" mode (QNM; Bruker Corp.), the tip vibrates at a fixed frequency of 2 kHz towards the sample and touches the surface with an ultralow force during each cycle. During approach and retraction, force–distance curves are recorded, which can be determined together with the topography and the following properties: adhesion force, energy dissipation, maximum force, hardness (DMT modulus), deformation, stiffness, and phase shift of oscillation at every image point. The instrument and its analysis software deliver a mapping of each property. With a conductive tip in tapping mode, the current during contact can also be measured at each point; previously, conductivity was measured in the so-called contact mode, which was associated with significant pressure on the sample. Statistical evaluation of the properties of each image was performed, yielding a histogram of the occurrence of the value for a specific property. The peak occurrence values were taken as mean values of the property. From several images, a general mean value for a property was calculated, with the corresponding error for one standard deviation.

The samples for the AFM investigation were all cut from the same position, at the 4 MEAs close to the hydrogen inlet of the cell. From the N115 a second sample was cut for comparison reasons, at a larger distance from the hydrogen inlet. For the AFM measurements, the twin MEAs were carefully separated manually and attached to the sample holder with adhesive tape. For current measurements, the samples were stored in Millipore water. For ionic conductivity measurements, the GDL was removed and samples were put with their electrodes on a porous, conducting, hydrophilic layer that provided a water supply to the back electrode. The schematic diagram of the AFM observation of the interface between the two semi-CCMs is shown in Fig. 2. In addition to inspection of the inner interface surfaces, MEA cross-sections performed by cryo-cleavage in liquid nitrogen were investigated using the QNM mode.

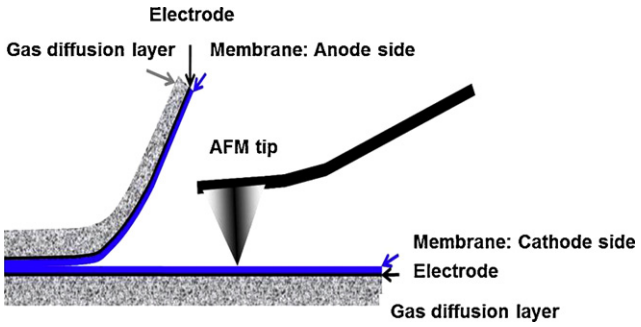

Fig. 2. Schematic representation of the AFM measurement performed on the inner membrane interfaces.

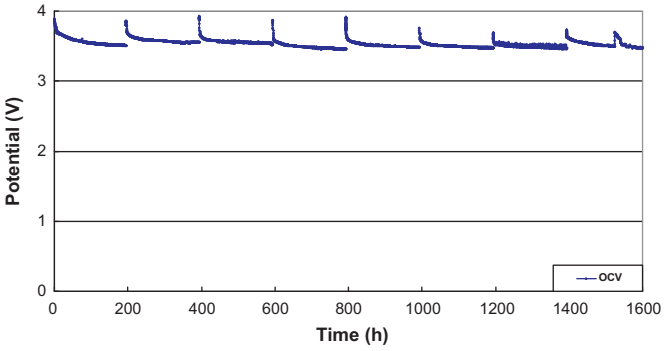

Fig. 3. Time evolution of the OCV of the stack during 1600 h of operation at OCV.

3. Results and discussion

3.1. In situ diagnosis

3.1.1. OCV time dependence

Fig. 3 shows the time evolution and decrease in OCV of the stack during the 1600 h of the experiment, associated with degradation processes. Throughout the experiment, OCV declines greatly for each time interval. This is in accordance with previous observations by Sahin et al. [14]. The initial OCV at the beginning of each session remains almost the same for up to 800 h, although the end OCV of each session is low and decreases with time. After about 800 h, the recovered OCV value at the beginning of the time interval decreases significantly. This sizeable voltage loss indicates that the component properties are degrading and thereby influencing the cell's functionality. During the last 200 h of OCV operation, an unexpected gas supply failure causes a shutdown, leading to similar time behaviour for the OCV.

By comparing the OCV time records for each individual cell shown in Fig. 5, it was found that OCV decay was not uniform among the four cells. The thinner membranes experienced a more serious voltage decrease than the thicker ones. For example, with the thinnest membrane, the OCV of Cell 4 decreased to below 0.8 V after 1600 h. The most significant decrease in this cell occurred during the last 600 h. However, the OCV of Cells 1 and 2, with their thicker membranes, showed a very stable trend during the whole degradation period. In addition, voltage fluctuations were observed after 1200 h, especially for the fuel cells with thinner membranes (Cells 3 and 4), which should be indicative of membrane deterioration.

3.1.2. Evolution of current voltage curves

Fig. 4 shows the V(I) curves of the cell stack after potential OCV holding for different durations, compared with the baseline. The relatively low performance of the stack was most probably due to the higher resistance of the double-layered thick membranes.

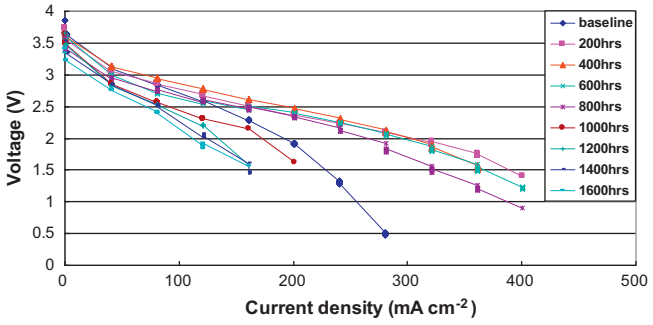

Fig. 4. IV curves of the cell stack after potential holding for different durations, compared with the baseline.

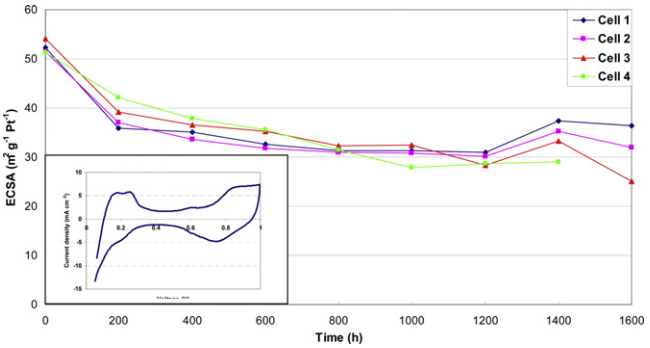

Fig. 6. Comparison of the calculated ECSA for each single cell, obtained from the CV test, for different durations; the inset is a typical CV curve (baseline of Cell 1).

After the first 200 h, the stack performance showed a significant improvement compared with the baseline after the conditioning. This indicates that the stack was not fully activated, although a conditioning process of 22 h had been conducted. Due to the double-sized membrane thickness, especially for Cell 1, more conditioning time might be needed. During the subsequent 600 h, the stack performance experienced a minor decrease. Then, the performance drop became more pronounced after 1400 and 1600 h of operation.

Fig. 5 compares the potential of each cell at OCV and 160 mA cm^{-2}. During the whole experimental period, the performance of the stack was limited by Cell 1, which contained the thickest membrane, N117. As the limiting current density was found to decrease during operation, a rather low current density of 160 mA cm^{-2} (the limiting current density of Cell 1 in the last V(I) curve) was chosen for comparing the cells. Fig. 5 demonstrates that at the beginning of the test OCV is higher for thicker membranes (Cells 1 and 2), corresponding to the lower hydrogen crossover rates through thicker membranes. With increasing operation time, the cells with thicker membranes showed more stable OCV than those with thinner membranes (Cells 3 and 4) as there are more materials to degrade before pinholes form for thicker membranes. A rapid OCV decrease occurred for Cell 4 (with the thinnest membrane) after about 1400 h, followed by Cell 3 (with the second thinnest membrane) after 1600 h due to membrane thinning or pinhole formation through thinner membranes. This observation confirms that membrane thickness determines cell durability under OCV conditions.

The time dependence of the cell voltages at 160 mA cm^{-2} showed pronounced differences compared to OCV behaviour. The lowest cell performance was observed at Cell 1 that contained the thickest membrane due to the large membrane resistances. The voltages of the cells increased during the first 400 h, especially for the cells with thicker membranes (Cells 1 and 2). The performance of Cells 1 and 2 showed obvious improvement of about 100 mV. However, the improvement in Cells 3 and 4 were minor, even within the range of measurement error. These results also confirmed that the evident performance enhancement of the stack during the first 200 h was mostly contributed by the cells with thicker membranes. Already after 400 h of operation, Cell 1 experienced a stronger performance loss compared to the other three cells, which was opposite to the OCV degradation trend. Since no strong increase in gas crossover was observed for Cell 1, the most probable reason for the performance loss should be either electrode degradation or gas diffusion layer degradation. As shown by the ECSA degradation curves in Fig. 6, no evidence was shown that catalyst surface area change was relevant to the performance loss. However, after the degradation test, remarkable GDL damages due to the compression on Cell 1 and Cell 2 (especially for Cell 1) were observed with naked eye. The shape of the flow field was clearly embedded into the GDL. While for cells with thinner membranes (Cell 3 and Cell 4), no such phenomenon was observed. Therefore, serious GDL deterioration of the CCM with doubled thicker membranes may be the reason for the unexpected performance loss trend observed in Fig. 5. This confirms that cell performance degradation is influenced by many factors, including cell components (membrane, catalyst, GDL), component design, and cell configuration.

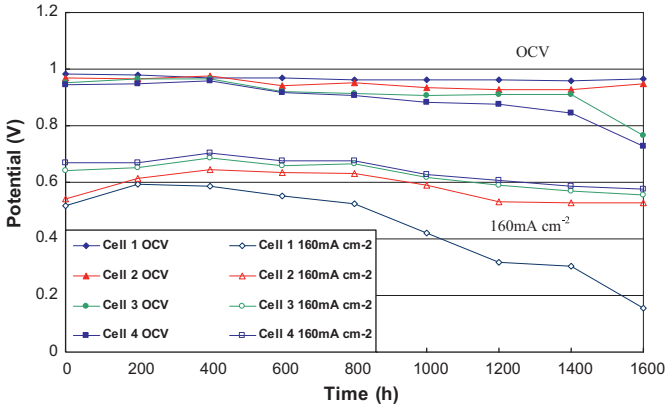

Fig. 5. Performance comparison of each single cell for different durations, at OCV and 160 mA cm^{-2}, respectively.

3.1.3. *Time dependence of cyclic voltammetry*

Commonly, the ECSA attained from CV measurement is used as an indicator of catalyst layer performance. Fig. 6 compares the calculated ECSA for each cell obtained from the CV test. The inset is a typical CV curve obtained from the baseline of Cell 1. The last CV measurement for Cell 4 was not obtained due to the excessive hydrogen crossover current. The ECSAs of all cells decreased with increasing OCV holding time. The reason for the ECSA decrease was Pt dissolution/redeposition, as well as possible corrosion of carbon support [6]. Pt evolution within the twin-CCM after the degradation test will be discussed in Section 3.2. ECSA loss was highest during the first 200 h, and then levelled off to a loss of about 45% after 1200 h. This behaviour was also found in our previous degradation research under OCV stress and idle conditions. However, the ECSA values after 1400 and 1600 h showed an unexpected increase compared with prior measurements. Considering the operating record of the test, the most plausible reason for this ECSA change is instrumental difference, as the last two tests were conducted with a second test station; consider that a movement of the stack involves release and tightening of the alignment, which might cause differences even in calibrated identical test stations. The ECSA measurements reflect the stronger decrease in performance of Cell

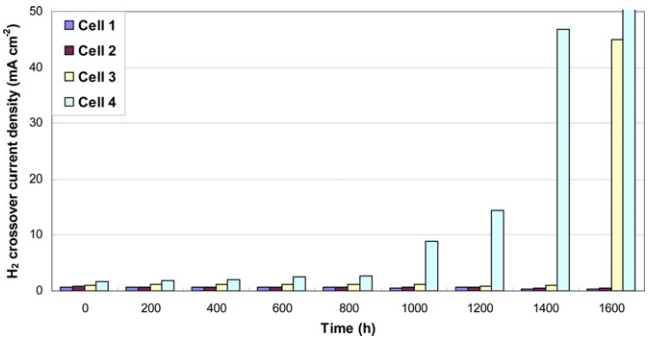

Fig. 7. Comparison of the hydrogen crossover current densities of each single cell at 0.5 V after each time interval during OCV operation.

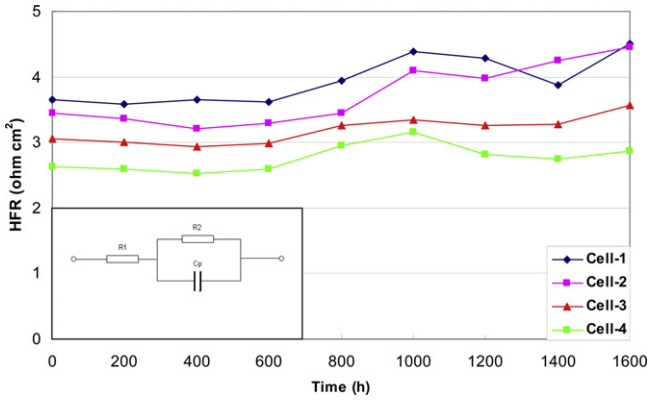

Fig. 8. HFR change of each single cell before and after each OCV degradation time interval; the inset is a typical equivalent circuit for a PEM fuel cell.

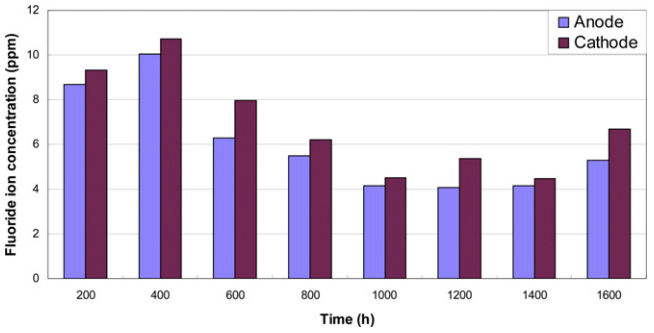

Fig. 9. Fluoride concentration of effluent water during OCV holding test, for both anode and cathode sides.

1, which may indicate that other factors, like deformation of the GDL, are important.

3.1.4. Time dependence of hydrogen crossover, determined by LSV

The hydrogen crossover current densities for each cell at 0.5 V after each time interval are compared in Fig. 7. For the thicker membranes (Cells 1 and 2) there were no significant changes in hydrogen crossover during the 1600 h, while the LSV curves showed a remarkable change for Cells 3 and 4, with their thinner membranes. The hydrogen crossover current increased with the relative decrease in membrane thickness (see Table 1 and description below). A huge increase in the hydrogen crossover current of Cell 4, with the thinnest membrane, happened after 1000 h of OCV holding. The current increased further, continuously, until the current value exceeded the instrument limit (2.5 A). Note that, Cell 3 showed an abnormal high increase in hydrogen crossover current at a later time, 1600 h, compared to the continuously increasing hydrogen crossover trend for Cell 4. This may be related to the stack transfer to another test station after 1200-h test. Nevertheless, membrane thickness plays a key role in fuel cell durability under OCV conditions. This coincides with the results of our previous experiments [12,13]. Therefore, although the cell with a thinner membrane may achieve a higher performance under the same working conditions, its life span is relatively short compared to cells with thicker membranes when exposed to the same stressors.

3.1.5. Time-dependent EIS measurements

The high frequency resistance (HFR) values of the EIS for the cells are compared in Fig. 8. The equivalent electrical elements can be determined from the EIS data using a fit to a typical equivalent circuit, shown in the inserted graph, where R_1 represents the HFR, R_2 represents the charge transfer resistance, and C_p represents the charge transfer related double-layer capacitance. Generally, the HFR is used to characterize the ohmic resistance of a PEM fuel cell, which is contributed by membrane resistance, by electronic resistance in the flow plates, current collectors, and gas diffusion media, and by contact resistances. Apart from membrane resistance, the other factors can be assumed to remain constant in this experiment. According to the data, all 4 cells showed a moderate increase in HFR. The baseline determination of HFRs (at 0 h) showed the expected rise with membrane thickness, which confirms that the HFR relates strongly to the membrane resistance. After the first 200 h of OCV operation, the HFR for all of the 4 cells decreased slightly, which may result from a better membrane humidification as mentioned in Section 3.1. The HFR change after 1000 h is believed to have resulted from the combined effects of membrane thinning and membrane structure deterioration. These two effects were confirmed by SEM and AFM observations, respectively, which will be presented in detail in Section 3.2. Membrane thinning and membrane structure deterioration might function in reverse ways: the former might decrease the resistance due to changes in the membrane's physical features, while the latter might increase the resistance due to structural changes in the Nafion® ionomer. Besides this, transfer between the two test stations might also have influenced the impedance test. Therefore, the trends in HFR for the 4 individual cells are not clear for this period. However, each end of test (EOT) resistance is higher than that at the beginning of the test (BOT).

3.2. Ex situ diagnoses

3.2.1. Time evolution of fluoride loss

The fluoride concentration was determined by measuring the effluent water during the OCV holding test for both anode and

Table 1
Membrane thickness comparison between fresh and degraded single cells.

Unused (μm)		Anode			Cathode		
		Degraded (μm)	Loss (μm)	Decrease (%)	Degraded (μm)	Loss (μm)	Decrease (%)
Cell1N117	183	171	12	6.5	160	23	12.6
Cell2N115	127	115	12	9.5	88	39	33
Cell3N212	50.8	43	7.8	15.4	23.6	27.2	53.5
Cell4N211	25.4	16	9.4	37	11.3	14.1	55.5

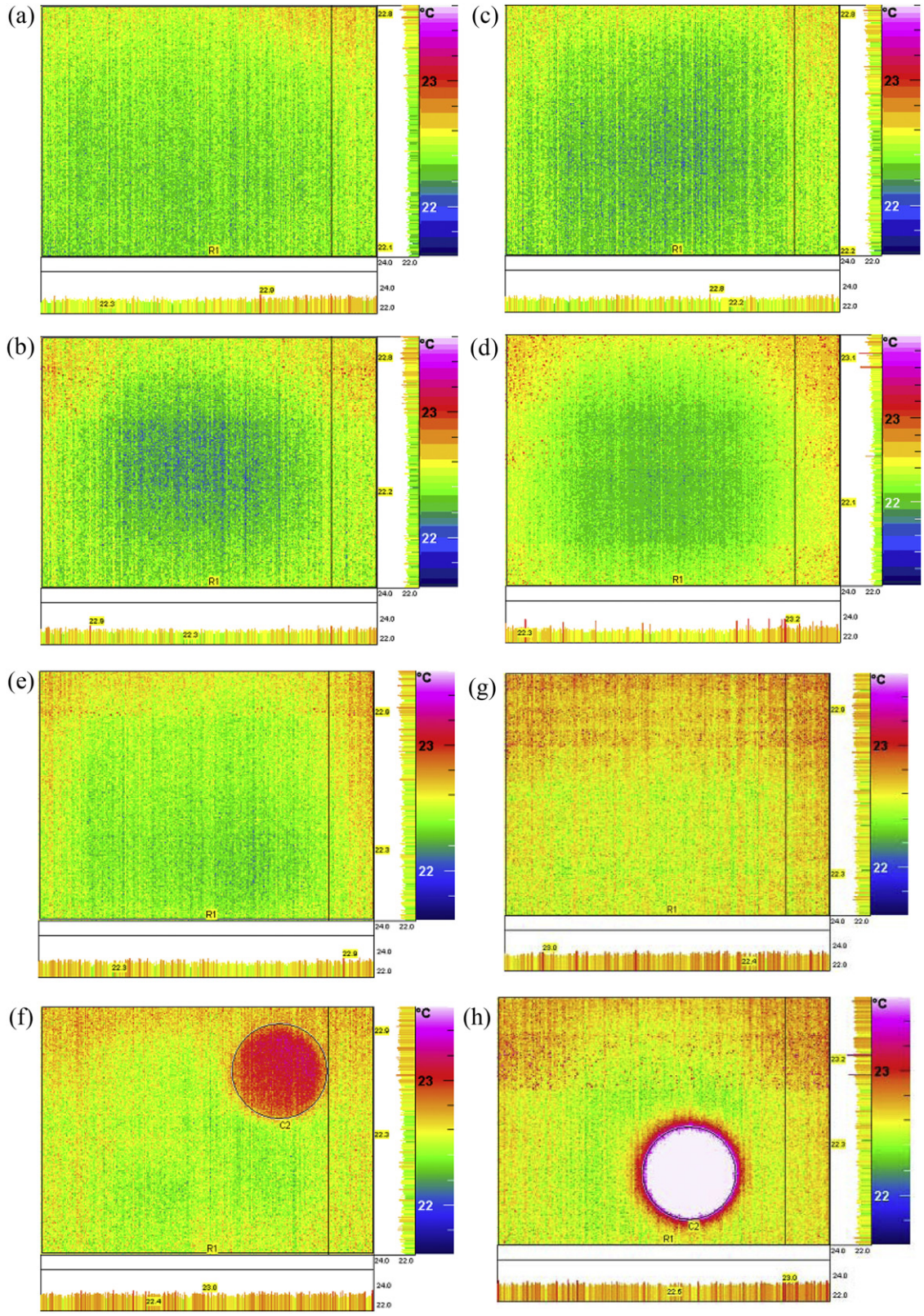

Fig. 10. IR images of fresh and degraded single cells: (a) unused Cell 1; (b) degraded Cell 1; (c) unused Cell 2; (d) degraded Cell 2; (e) unused Cell 3; (f) degraded Cell 3; (g) unused Cell 4; (h) degraded Cell 4.

cathode sides. Due to the long experimental time, it was difficult to collect all the accumulated exhaust water. Therefore, water samples were periodically collected, and only relative fluoride loss is presented instead of accumulative fluoride loss. As shown in Fig. 9, the cathode side exhaust water contained more fluoride than the anode side exhaust water, which can be interpreted as indicating a stronger ionomer degradation on the cathode side. This is further confirmed by the SEM results below. Although degradation of the

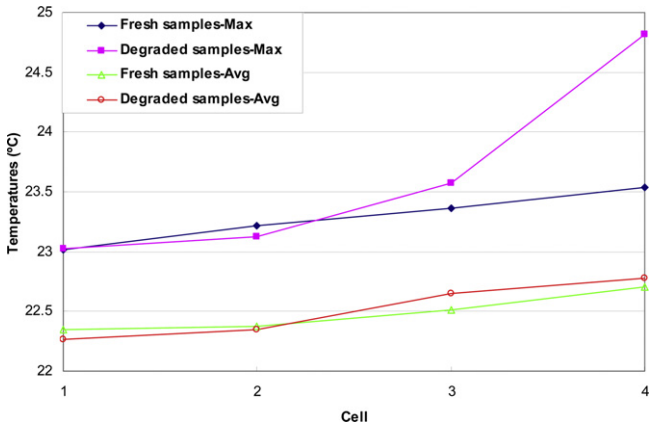

Fig. 11. Temperature differences for the unused and degraded samples in the IR images (average and maximum temperatures).

catalyst layer ionomer might also contribute to fluoride loss, the main source of the fluoride is considered to be membrane ionomer degradation, based on its predominant mass and membrane thinning, as observed by SEM (see Table 1).

3.2.2. IR imaging of pinhole formation

According to the images from the IR camera, shown in Fig. 10, the average temperatures of the aged MEAs from Cells 1 and 2 were similar to those of the unused cells. For Cells 3 and 4, hot spots were detected on the degraded samples, in contrast to their original uniform temperature distribution. Hot spots are certain areas with a higher temperature due to increased oxygen/hydrogen reaction based on their crossover amount through the weaker and thinner areas of the membrane. When hot spots occur, they indicate fatal degradation due to membrane thinning or pinhole formation. Therefore, the hot spots detected in Cells 3 and 4 confirmed that serious membrane damage was present in the cells with thinner membranes after ageing. The temperature differences between the unused and aged samples are displayed in Fig. 11. The average temperature differences reflect the same trend for different cells, but the maximum temperature differences are huge for Cells 3 and 4. This indicates that the majority of the membrane is still in normal condition while occasionally weakened areas result in hot spots. Note that both the average and the maximum temperatures for the unused samples are higher for thinner membranes. The temperature difference between the thickest and the thinnest is within 0.5 °C, which proves that IR imaging is a useful diagnostic tool to detect PEM integrity.

3.2.3. Structural investigations using SEM

SEM images of the cross-sectioned MEA after the degradation test are shown in Fig. 12. As labelled, the cathodes sides are at the top of these images. For each MEA, the boundary of the two semi-layers is clearly identified in the SEM images, as marked by arrows. Before operation, the thicknesses of the two membrane layers are equal. After the OCV holding test, the thicknesses of the two membranes are no longer identical. The membrane thinning of the semi-CCM near the cathode side is greater than near the anode side, which coincides with the higher fluoride loss mentioned previously. This might be the result of the different crossover rate of hydrogen and air through the PEM. Ogumi et al. [18] found that under the same conditions, the crossover rate of oxygen is about half the rate of hydrogen through Nafion® 125 membrane (with

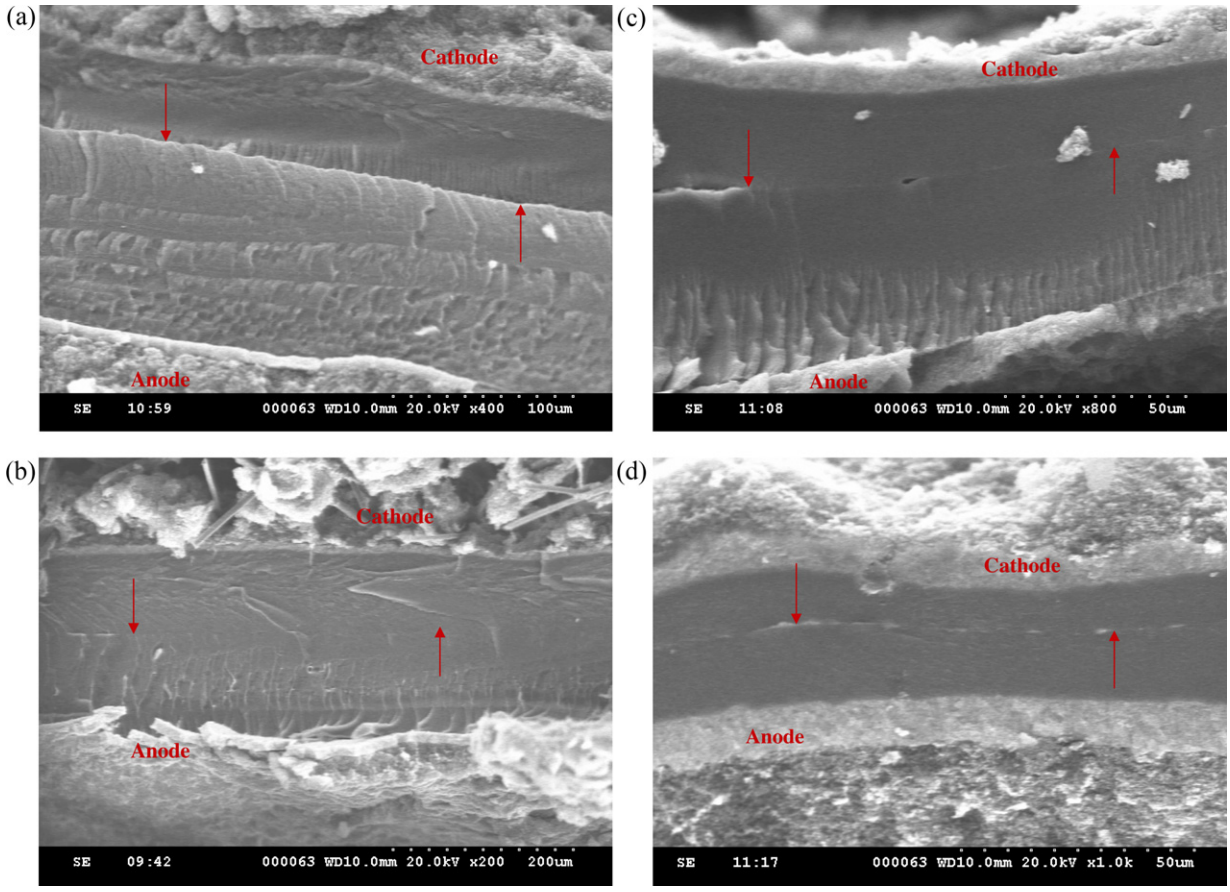

Fig. 12. SEM images of each degraded single cell: (a) Cell 1; (b) Cell 2; (c) Cell 3; (d) Cell 4.

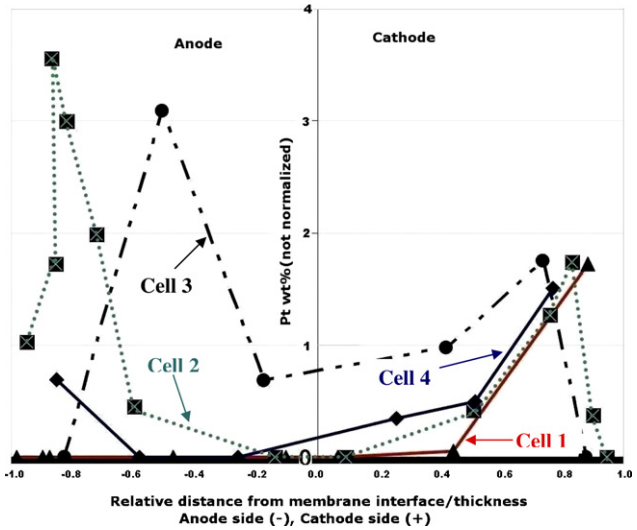

Fig. 13. Pt content of the cross section of Cell 3 determined by EDX.

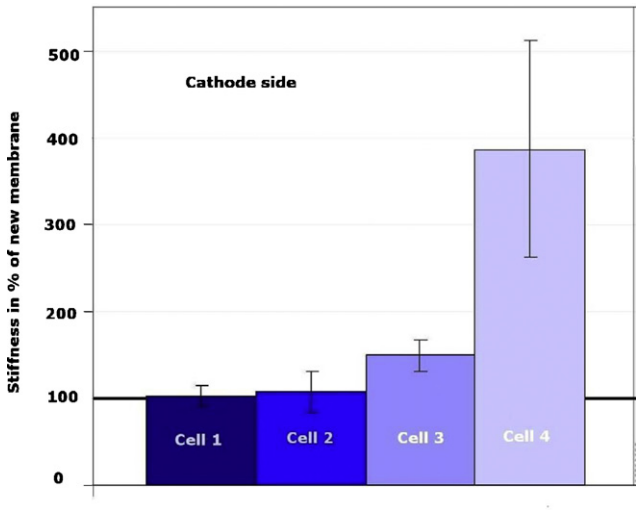

Fig. 15. Statistical evaluation of the stiffness of the membrane surfaces in relation to the corresponding unused membrane.

a thickness of 125 μm) at 25 °C. High membrane degradation due to radical formation of oxygenated species is expected at areas of high oxygen partial pressure in the presence of hydrogen and Pt catalyst (high peroxide rates are found in the hydrogen adsorption region of Pt). Therefore, stronger cathode-side membrane thinning can be expected. The thickness losses for each cell are listed in Table 1, together with thickness comparisons for the degraded and the unused membranes. The thicknesses of the individual single-layer membranes of the unused samples are also given. For the aged membranes, average values obtained from 5 random spots for each sample are listed, because the thinning is not even along the whole cross-section direction. Comparison of the 4 cells shows that the absolute thickness loss for Cells 1 and 2 is larger than for Cells 3 and 4. However, the relative thickness change is larger for the thinner membranes, leading to a relative membrane loss order of Cell 1 < Cell 2 < Cell 3 < Cell 4. This further confirms the results obtained using IR imaging—pinholes are more prone to develop in Cells 3 and 4, with their high percentage of thickness loss.

Besides the general SEM investigations, high-resolution SEM-EDX was used to test the Pt content within the membranes. As

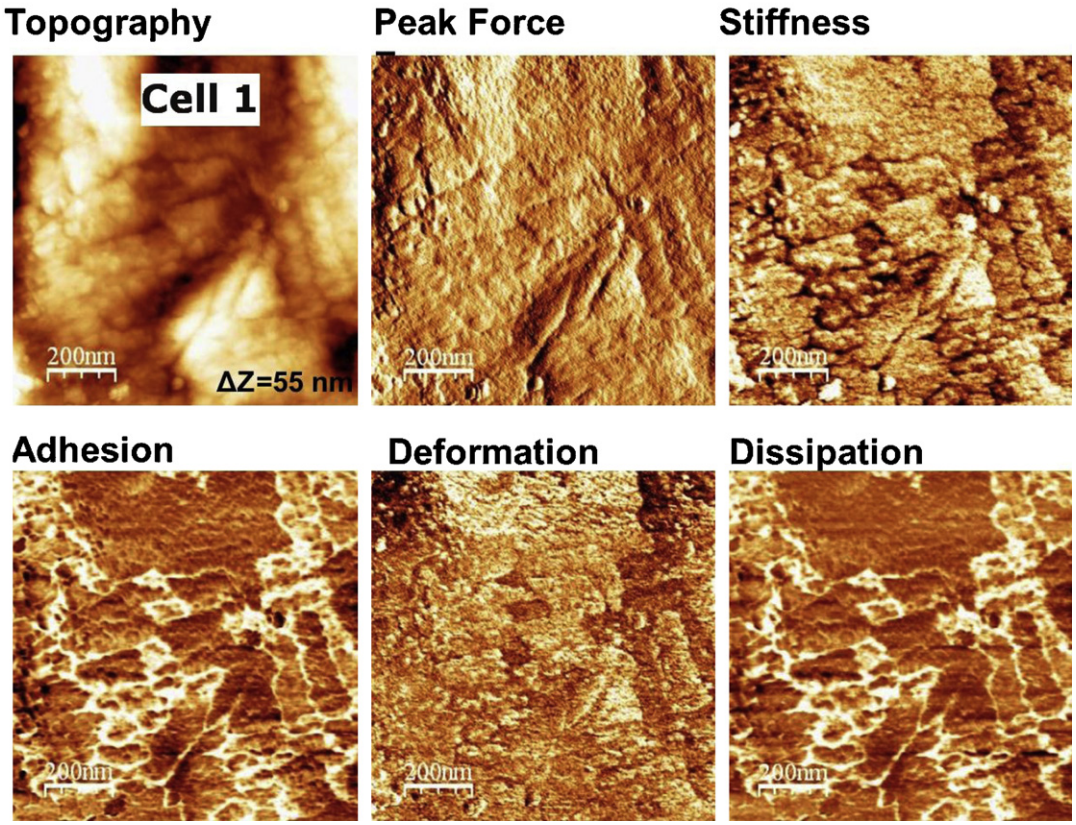

Fig. 14. Typical AFM images of topography, together with mapping of peak force, stiffness, adhesion, deformation, and dissipation, obtained using QNM tapping mode from the force-distance curves on Cell 1 membrane surfaces after 1600 h OCV operation on the cathode side.

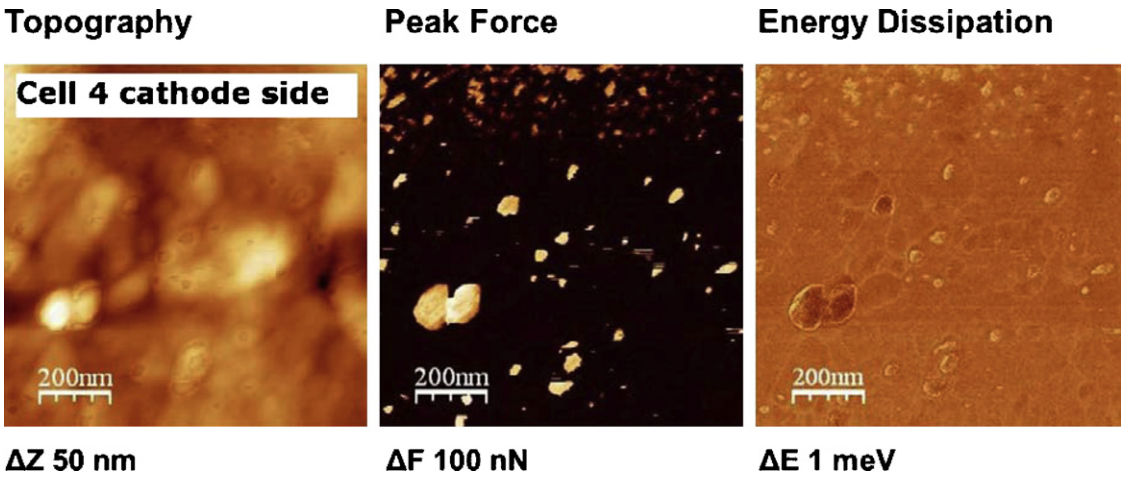

Fig. 16. AFM images by HarmoniX mode on Cell 4 membranes at the cathode side.

shown in Fig. 13, Pt was detected in different quantities all over the membrane cross-sections. However, there is no clear trend in the distribution of the Pt throughout the membranes, even though the chosen positions were all same for the four samples. Similar Pt redeposition behaviour (Pt band in membrane) has been observed, and the reasons for such Pt migration have also been investigated by other researchers [19,20].

3.2.4. AFM

All 8 inner interfaces of the 4 cells were investigated using the HarmoniX and QNM modes. In Fig. 14, the surface structure of the Cell 1 membrane (N117) measured by QNM is shown, together with the mapping of peak force, stiffness, adhesion force, deformation, and energy dissipation of the surface, in a similar way as was found for all membrane surfaces of the stack. In the adhesion force image—which is extremely surface sensitive—surface material heterogeneities are visible. The surface areas with a high adhesion force are the topmost layers (in the topography image), exhibit higher energy dissipation, are more deformable, and are more brittle (lower stiffness). In the peak force image, no difference in hardness is visible. These aged surfaces appear to have flakes peeling off the surface and exposing a fresher surface beneath. In addition, particles were frequently detected, mainly at the inner cathode-side interfaces of the thinner membranes.

Fig. 15 presents a comparison of the mean stiffness of the cathode side relative to an unused membrane of the same type, at the inner interface of the 4 membranes, together with error bars. The stiffness images were measured using the QNM mode. A clear exponential increase in stiffness from the thicker to the thinner membranes is visible. Enhanced stiffness is expected for a degraded polymer, and the AFM results underline the accentuated ionomer degradation of the thinner membranes, in accordance with the results for H_2 permeability. In Fig. 16, the particles detected in the inner interfaces, here at the Cell 4 cathode side, are further investigated. The most likely interpretation of the nature of most of these particles is that they are redeposited Pt, as shown by the HarmoniX mode measurements. In comparison to Nafion®, Pt is very hard (peak force image) and has a smaller energy dissipation due to its higher elasticity. Pt particles were also detected on cross-sections of the membrane. Fig. 17 shows a few large Pt particles on the cross-section of the Cell 3 membrane in the topography image. Overlaying the adhesion force mapping onto the topography clearly shows very thin extended Pt layers covering a large fraction of the surface, identifiable by their small adhesion force.

In Fig. 18, current measurement performed in contact mode for Cell 3 shows high conductivity, but still exposes non-conductive areas in the 1.5 μm image on the left side. The conductivity images are in principle similar to the new membrane samples reported in various previous studies [21–24]. However, the conductivity areas are large here and the conductivity is higher. In addition, interpenetrating regions with different current levels (>3) are present, which have not been detected before. A histogram of the current levels is

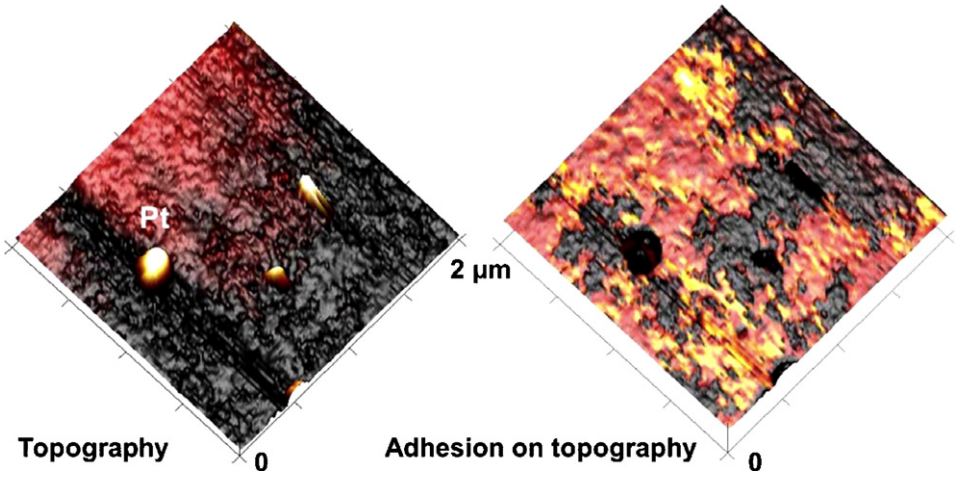

Fig. 17. QNM images of a cross-section of Cell 3, with superimposition of topography and adhesion.

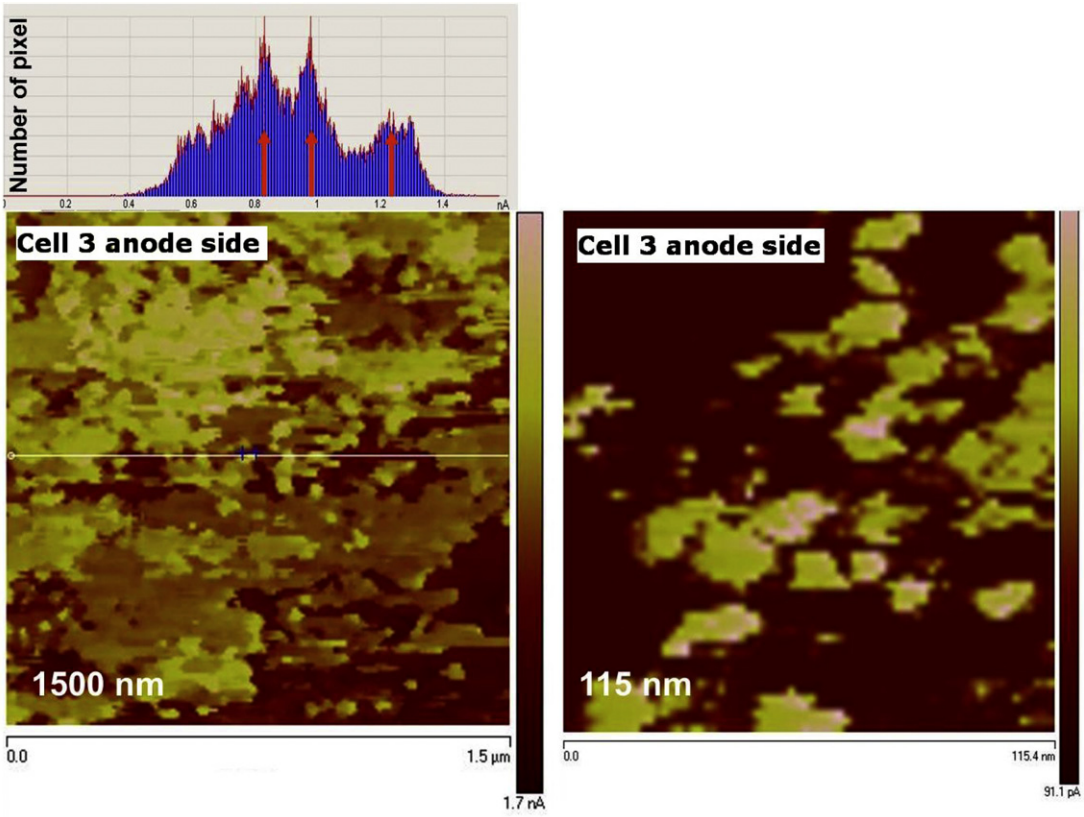

Fig. 18. Conductive AFM current images in contact mode of Cell 3 at the anode side, showing conductivity distribution on the membrane surface for 1.5 μm × 1.5 μm (left) and 115 nm × 115 nm (right). The histogram on top shows the occurrence in pixels of current values for the whole image.

given in the upper left of Fig. 18. It is well known that the ionic network of Nafion® consists of branched conductive channels. Areas of similar current values are most likely interconnected through a branched ionic subnet. Regions with the same conductivity belong to the same ionic subnet and might have only a high resistive connection with a high resistance beneath the surface. The subnets are an indication of a non-uniform conductive network, probably caused by the activation process of the membrane at the start of fuel cell operation. Also, the rather high total conductivity is due to the extended activation of the aged membranes in comparison to the unused membranes. On the right side, a high resolution image is shown with small conductive areas of about 10 nm, and even some smaller spots of only a few nanometers. In previous studies, the smallest conductive structures were assigned to individual inverted micelles as part of a conductive network of Nafion®. These micelles cluster into large structures of 10–30 nm, also seen in the aged samples.

4. Conclusions

Using in situ and ex situ diagnostic tools, the effect of OCV operation as an accelerated mode of PEM degradation in a 4-cell stack with twin-CCMs was investigated. Different membrane thicknesses, namely N117, N115, N212, and N211, were used in the 4-cell stack. The results showed performance loss and OCV loss during OCV degradation for up to 1600 h, differing widely for the various cells. Disproportionately high OCV loss and hydrogen crossover were observed for the two thinnest membranes, confirmed by IR measurements and thinning detected by SEM analysis. The functionality loss in the cells with thin membranes was associated with strong thinning and even pinhole formation. On the other hand, performance loss at 160 mA cm^{-2} was more pronounced for cells with thicker membranes. The active Pt surface area decreased strongly at the beginning of the OCV, in accordance with previous studies. For stack functioning, membrane degradation is more serious than electrode degradation under OCV conditions. Investigation of cross-sections using SEM indicated stronger thinning at the cathode side. Further investigations with novel AFM methods revealed that the aged inner membrane surfaces were significantly stiffer, in particular for the thinner membranes, and had a degraded surface structure with polymer flakes. These results supported the electrochemical results. The local ionic conductivity, however, was found to be higher compared with previous investigations of unused samples. An interpenetrating ionic network with different current levels was found at the inner interfaces.

References

[1] W. Liu, D. Zuckerbrod, J. Electrochem. Soc. 152 (2005) A1165–A1170.
[2] T.A. Aarhaug, A.M. Svensson, ECS Trans. 3 (2006) 775–780.
[3] A. Ohma, S. Suga, S. Yamamoto, K. Shinohara, J. Electrochem. Soc. 154 (2007) B757–B760.
[4] V. Mittal, H.R. Kunz, J.M. Fenton, ECS Trans. 1 (2006) 275–282.
[5] B. Sompalli, B.A. Litteer, W.B. Gu, H.A. Gasteiger, J. Electrochem. Soc. 154 (2007) B1349–B1357.
[6] S. Zhang, X.-Z. Yuan, J.N.C. Hin, H. Wang, K.A. Friedich, M. Schulze, J. Power Sources 194 (2009) 588–600.
[7] A. Collier, H. Wang, X.-Z. Yuan, J.J. Zhang, D.P. Wilkinson, Int. J. Hydrogen Energy 31 (2006) 1838–1854.
[8] H.L. Tang, P.K. Shen, S.P. Jiang, F. Wang, M. Pan, J. Power Sources 170 (2007) 85–92.
[9] S.A. Vilekar, R. Datta, J. Power Sources 195 (2010) 2241–2247.
[10] W. Yoon, X. Huang, J. Electrochem. Soc. 157 (2010) B599–B606.
[11] J. Wu, X.-Z. Yuan, J.J. Martin, H. Wang, D. Yang, J. Qiao, J. Ma, J. Power Sources 195 (2010) 1171–1176.
[12] X.-Z. Yuan, S. Zhang, H. Wang, J. Wu, J.C. Sun, R. Hiesgen, K.A. Friedrich, M. Schulze, A. Haug, J. Power Sources 195 (2010) 7594–7599.
[13] S. Zhang, X.-Z. Yuan, J.N.C. Hin, H. Wang, J. Wu, K.A. Friedrich, M. Schulze, J. Power Sources 195 (2010) 1142–1148.

[14] O. Sahin, S.I. Maganov, C. Su, C. Quate, O. Solgaard, Nat. Nanotechnol. 2 (2007) 507–514.
[15] O. Sahin, C.F. Quate, O. Solgaard, A. Atalar, E.L. Ginzton, Phys. Rev. B 69 (2004), 165416-1-9.
[16] O. Sahin, Phys. Rev. B 77 (2008), 115405-1-6.
[17] O. Sahin, Rev. Sci. Instrum. 78 (2007), 103707-1-4.
[18] Z. Ogumi, T. Kuroe, Z.-I. Takehara, J. Electrochem. Soc. 132 (1985) 2601–2605.
[19] W. Bi, G.E. Gray, T.F. Fuller, Electrochem. Solid-State Lett. 10 (2007) B101–B104.
[20] P.J. Ferreira, G.J. la O', Y. Shao-Horn, D. Morgan, R. Makharia, S. Kocha, H.A. Gasteiger, J. Electrochem. Soc. 152 (2005) A2256–A2271.
[21] R. Hiesgen, I. Wehl, E. Aleksandrova, E. Roduner, A. Bauder, K.A. Friedrich, Int. J. Energy Res. 34 (2010) 1223–1238.
[22] R. Hiesgen, E. Aleksandrova, G. Meichsner, I. Wehl, E. Roduner, K.A. Friedrich, Electrochim. Acta 55 (2009) 423–429.
[23] D.G. Sanchez, D.G. Diaz, R. Hiesgen, I. Wehl, K.A. Friedrich, J. Electroanal. Chem. 649 (2010) 219–231.
[24] E. Aleksandrova, R. Hiesgen, D. Eberhard, K.A. Friedrich, T. Kaz, E. Roduner, ChemPhysChem 8 (2007) 519–522.